PHYSICAL REVIEW A VOLUME 43, NUMBER 5 1 MARCH 1991

Mg 3*pns* and 3*pnd* ($J = 1$) autoionizing series

G. W. Schinn, C. J. Dai, and T. F. Gallagher
Department of Physics, University of Virginia, Charlottesville, Virginia 22901

(Received 18 September 1990)

The Mg 3*pns* ($n = 10-18$) and 3*pnd* ($n = 9-40$) doubly excited $J = 1$ autoionizing states have been observed experimentally using an isolated-core excitation method with stepwise laser excitation. Linearly polarized laser light excites the 3*pnd* $J = 1$ and $J = 3$ states, as well as the 3*pns* $J = 1$ states. Our previous study of the $J = 3$ states enables the $J = 1$ states in the 3*pnd* spectra to be identified. We have also calculated the spectra from a reaction matrix, and the agreement between theory and experiment is generally excellent. Differences between the $J = 1$ and $J = 3$ features are discussed and qualitatively explained in terms of semiclassical arguments. Additionally, energies of the 3*sns* $^1S_0$ ($n = 11-22$) Rydberg levels are reported.

INTRODUCTION

The members of an autoionizing Rydberg series, like their counterparts in bound Rydberg series, may be treated in a unified fashion using multichannel quantum-defect theory[1,2] (MQDT) when analyzing their interactions with other series and the continua in which the series is embedded. However, in contrast to a bound Rydberg state, for which the most interesting characteristics derive from the large-radius behavior of the Rydberg electron's wave function, the important properties of an autoionizing Rydberg state arise from interactions of the outer electron's wave function in the atomic-core region. It is in this small-*r* region that the energy and angular momentum exchange necessary for autoionization occurs. Indeed, the total angular momentum of the doubly excited state can play a very important role in determining the autoionization rate.

We report here a study of the 3*pns* and 3*pnd* ($J = 1$) autoionizing states of magnesium, which, in conjunction with our recent investigation of the 3*pnd* ($J = 3$) states[3] (hereafter referred to as I), provides insight into the dependence of autoionization in the Mg 3*pnd* series upon total angular momentum. Additionally, we have measured term energies of the corresponding 3*sns* $^1S_0$ Rydberg series for states up to $n = 22$.

Preparation of doubly excited autoionizing states is effected using the isolated-core excitation (ICE) technique.[4] Numerous states may be produced with this excitation scheme, many of which cannot be excited by photoionization from the ground state on account of selection-rule restrictions. Additionally, with ICE there is virtually no direct continuum excitation, and hence the experimental spectra do not exhibit the Beutler-Fano interference effect[5] characteristic of photoabsorption spectra, which occurs when the amplitudes for continuum and doubly-excited-state excitation are similar.

The resulting spectra can be compared with spectra synthesized using an eigenchannel *R*-matrix calculation combined with the MQDT parameters appropriate to the transitions studied here.[6] This approach has proven remarkably successful in reproducing complicated spectra observed in ICE excitation of autoionizing series in the heavier alkaline-earth elements Ca (Ref. 7), Sr (Ref. 8), and Ba (Ref. 9). For each specified total angular momentum J and parity in the element of interest, a nearly energy-independent reaction matrix $\underline{K}$ must be calculated, which takes into account the effects on the core by the valence electrons. Most of the computational difficulty in reproducing the spectra is involved in the evaluation of this matrix. Once calculated, it can be used in conjunction with the appropriate angular momentum algebra and wave-function orthonormality considerations to synthesize the spectra arising from excitation from any initial state to an autoionizing state of the desired J and parity. In I, we successfully applied this procedure to the odd-parity $J = 3$ case in Mg using a $\underline{K}$ matrix calculated by Greene, and used those results, in combination with a similar calculation by Greene[10] for the odd-parity $J = 1$ case, to reproduce our spectra.

EXPERIMENTAL APPROACH

The frequency-doubled and frequency-mixed radiation from the three pulsed dye lasers is used in the three-step excitation scheme shown in Fig. 1. The first two steps excite one of the two valence electrons into either a 3*sns* or 3*snd* singlet Rydberg state. Following an appropriate time delay, the third laser beam excites the remaining valence electron on what is effectively the Mg$^+$ 3*s*-3*p* transition. The excitation radiation for all three steps is linearly polarized in the same direction. The electric-dipole selection rules limit the 3*pnd* doubly excited states to total angular momenta of either $J = 1$ or $J = 3$; members of the 3*pns* series clearly cannot have $J = 3$ and hence are further restricted to only $J = 1$.

Figure 2 shows the apparatus used in this experiment. It is essentially identical to that described in I, and so will only briefly be described here. A Quanta Ray DCR-1 Nd:YAG (where YAG denotes yttrium aluminum garnet) laser (not shown) is used to pump the three dye lasers. The output from the first of these lasers is doubled

TABLE I. Elements of the matrix blocks comprising the 7×7 block-diagonal K matrices calculated by Greene[a] corresponding to the three energies (in atomic units with respect to the Mg^{2+} ground-state limit) used in this analysis.

		$^1P^\circ$			$^3P^\circ$		$^3D^\circ$
Energy (a.u.)	$3s\epsilon p$	$3p\epsilon s$	$3p\epsilon d$	$3s\epsilon p$	$3p\epsilon s$	$3p\epsilon d$	$3p\epsilon d$
−0.40	−1.791 422 07	3.455 255 23	1.160 308 65	0.114 522 34	0.406 039 80	0.198 140 86	
	3.455 255 23	−6.456 068 24	−2.121 670 89	0.406 039 80	−2.312 831 03	0.037 063 04	0.582 377 58
	1.160 308 65	−2.121 670 89	−0.902 527 51	0.198 140 86	0.037 063 04	0.635 267 54	
−0.39	−1.880 631 94	3.637 936 51	1.186 988 76	0.092 347 99	0.422 902 43	0.190 380 44	
	3.637 936 51	−6.889 310 65	−2.176 173 66	0.422 902 43	−2.404 403 46	0.021 993 11	0.605 326 03
	1.186 988 76	−2.176 173 66	−0.869 989 01	0.190 380 44	0.021 993 11	0.633 640 82	
−0.38	−1.967 722 95	3.830 859 00	1.220 994 90	0.071 804 14	0.438 171 18	0.179 869 21	
	3.830 859 00	−7.368 134 10	−2.256 506 55	0.438 171 18	−2.494 359 10	0.006 215 19	0.632 968 65
	1.220 994 90	−2.256 506 55	−0.852 205 19	0.179 869 21	0.006 215 19	0.631 670 05	

[a] See Ref. 10.

in a potassium dihydrogen phosphate (KDP) crystal to generate the 285.3-nm radiation needed to excite the first resonance of neutral Mg. The second-laser output is mixed with the 1064-nm Nd:YAG fundamental in another KDP crystal to yield radiation in the 375–400-nm range, the particular wavelength depending upon the desired Rydberg-state n value. This beam is delayed to excite the atoms some 5 ns after the first laser beam. The output from the third laser is also doubled in a KDP crystal, and the $\simeq$280-nm wavelength scanned over an approximately 2-nm range across the two Mg^+ 3*s*-3*p* transitions. As the wavelength is scanned, the optimal phase-matching condition in the doubling crystal is servomechanically maintained. The path length of this light is adjusted in order that it interacts with the atoms about 10 ns after the second beam. To ensure that the three laser beams are polarized in the same direction, all three pass through linear polarizers before entering the vacuum chamber.

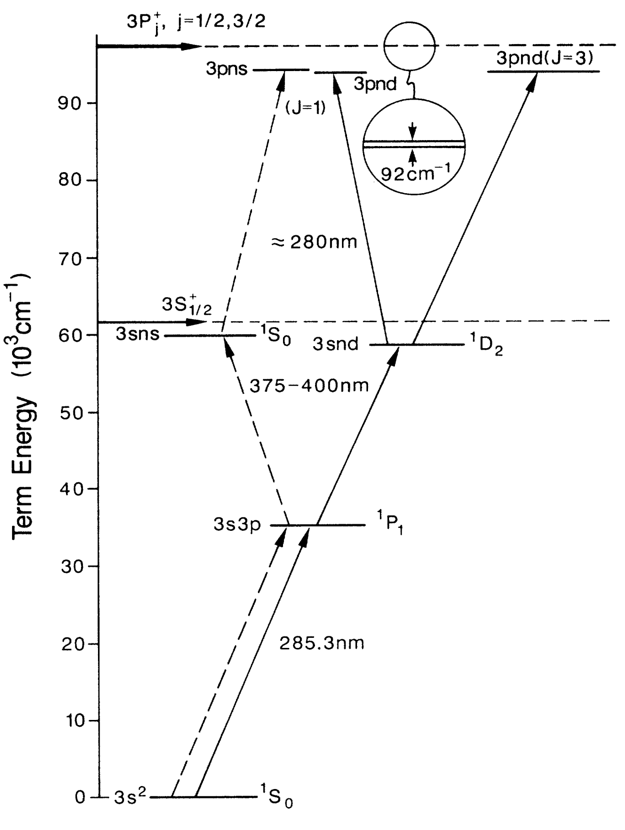

FIG. 1. ICE excitation scheme used in this experiment. One valence electron is prepared in a 3*snd* ($n=9$–40) or 3*sns* ($n=10$–18) Rydberg state, and the second electron is excited by the third step. All (frequency-doubled) laser beams are linearly polarized in the same direction, producing both $J=1$ and $J=3$ final states for the 3*pnd* case.

An atomic beam of Mg, emanating from a resistively heated oven, intersects the laser beams between two field plates separated by $\simeq 1$ cm. About 1 μs after the laser excitation, an approximately +9-V pulse on the bottom plate pushes the ions resulting from autoionization through a mesh on the upper plate, where they are subsequently detected by a particle multiplier. The ion signals are amplified, sent to a gated integrator, and then on to a microcomputer, which stores the data collected at the 12-Hz laser repetition rate.

The frequency of the third laser is corrected in the data analysis for scan nonlinearities and put on the absolute basis using the signals from an external étalon and Ar optogalvanic tube, respectively.

SYNTHESIS OF SPECTRA FROM THE $\underline{K}$ MATRIX

The procedure used to calculate the spectra from the $\underline{K}$ matrix is based upon that given by Greene and Kim[11] and Cooke and Cromer[12] (hereafter referred to as CC). This is in contrast to I, where instead of the CC approach applied here, the method of Lee and Lu[13] (hereafter referred to as LL) was used and discussed at some length. However, much of the theoretical framework is very similar, and was discussed at some length in I for the odd-parity 3*pnd* $J=3$ case. Hence we shall only outline how the odd-parity 3*pnd* $J=1$ and 3*pns* $J=1$ spectra were synthesized, emphasizing the differences between the LL and CC approaches. Of course, both procedures lead to iden-

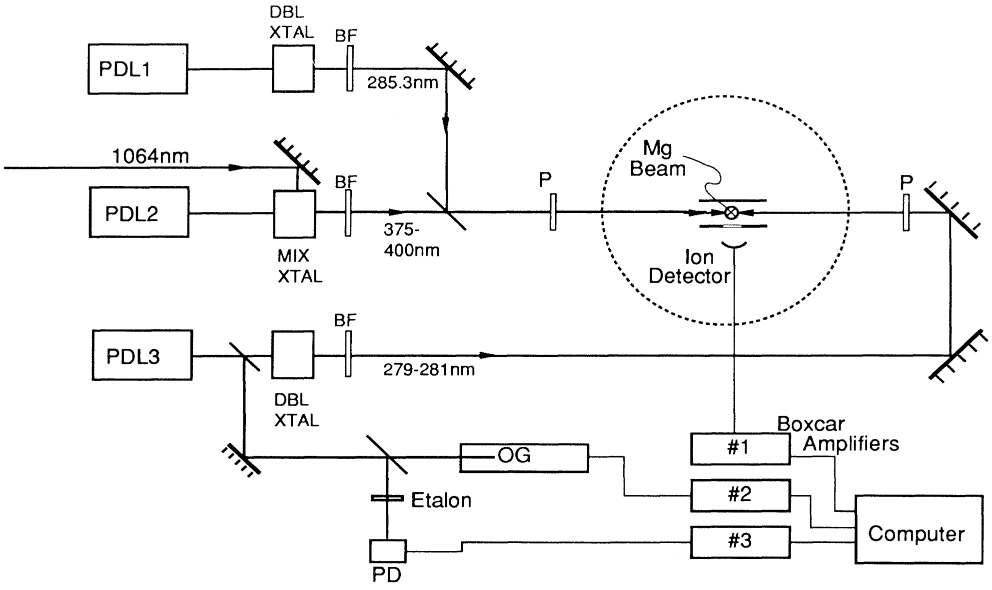

FIG. 2. Schematic of experimental setup, as described in text. PDL, Nd:YAG-pumped pulsed dye laser; BF, blocking filter passing only frequency-doubled radiation generated in crystal; OG, argon optogalvanic tube used to provide absolute frequency scale; PD, photodiode detecting étalon fringes to linearize scan; DBL CRYST, KDP doubling crystal; MIX CRYST, KDP mixing crystal.

tical results.

There are seven possible odd-parity $J=1$ channels below the Mg^{+} $3p$ states. They may be written as jj-coupled dissociation channels, or as LS-coupled channels, which are more appropriate for expressing the close-coupled eigenchannels. The associated transformation matrix may be evaluated using standard $3n$-j tables,[14] and is presented in Eq. (1) along with the basis sets it connects. The seven dissociation channels and their mutual interactions are shown schematically in Fig. 3. As discussed in I, the effect of configurations converging to higher Mg^{+} limits is expected to be negligible, and thus they are not included in the analysis.

Greene has evaluated the reaction matrices at three energies, for the three LS-coupled terms by which the odd-parity $J=1$ $3p\epsilon d$ and $3s\epsilon p$ configurations may be described. These energies, at -0.40, -0.39, and -0.38 a.u. below the lowest-lying Mg^{2+} limit, correspond to Mg term energies of 95 148.8, 97 343.5, and 99 538.3 cm^{-1}. In our calculations the block-diagonal energy-interpolated $\underline{K}^{LS}$ matrix is found by fitting a parabola to the values at these three energies. The blocks comprising each of these 7×7 matrices are presented in Table I.

The orthogonal 7×7 transformation matrix $\underline{V}$ needed to transform the LS-coupled states to the jj-coupled dissociation channels is given in Eq. (1):

$$\begin{array}{c} 3s_{1/2}\epsilon p_{1/2} \\ 3s_{1/2}\epsilon p_{3/2} \\ 3p_{1/2}\epsilon s_{1/2} \\ 3p_{3/2}\epsilon s_{1/2} \\ 3p_{1/2}\epsilon d_{3/2} \\ 3p_{3/2}\epsilon d_{3/2} \\ 3p_{3/2}\epsilon d_{5/2} \end{array} = \begin{bmatrix} \sqrt{\frac{1}{3}} & 0 & 0 & \sqrt{\frac{2}{3}} & 0 & 0 & 0 \\ \sqrt{\frac{2}{3}} & 0 & 0 & -\sqrt{\frac{1}{3}} & 0 & 0 & 0 \\ 0 & -\sqrt{\frac{1}{3}} & 0 & 0 & \sqrt{\frac{2}{3}} & 0 & 0 \\ 0 & \sqrt{\frac{2}{3}} & 0 & 0 & \sqrt{\frac{1}{3}} & 0 & 0 \\ 0 & 0 & \sqrt{\frac{1}{3}} & 0 & 0 & \sqrt{\frac{1}{6}} & \sqrt{\frac{1}{2}} \\ 0 & 0 & \sqrt{\frac{1}{15}} & 0 & 0 & \sqrt{\frac{8}{15}} & -\sqrt{\frac{2}{5}} \\ 0 & 0 & \sqrt{\frac{3}{5}} & 0 & 0 & \sqrt{\frac{3}{10}} & -\sqrt{\frac{1}{10}} \end{bmatrix} \begin{array}{c} 3s\epsilon p\ ^1P \\ 3p\epsilon s\ ^1P \\ 3p\epsilon d\ ^1P \\ 3s\epsilon p\ ^3P \\ 3p\epsilon s\ ^3P \\ 3p\epsilon d\ ^3P \\ 3p\epsilon d\ ^3D \end{array} . \quad (1)$$

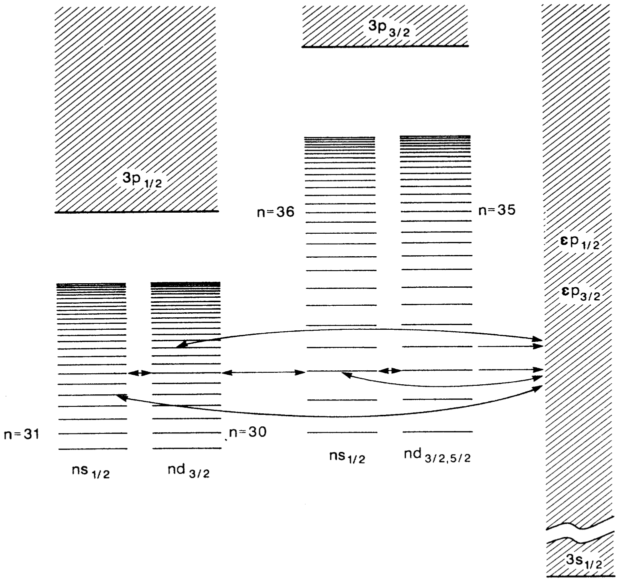

FIG. 3. Illustration of interseries interaction and continuum decay channels for the autoionizing Rydberg series studied here. Although shown here for high-n values, in the present experiment $3pns$ doubly excited states were excited only up to $n=18$.

$\underline{K}^{jj}$ may now be evaluated using the similarity transformation

$$\underline{K}^{jj}=\underline{V}^T\underline{K}^{LS}\underline{V} \ . \tag{2}$$

For simplicity, the seven jj-coupled dissociation channels in Eq. (1) are numbered from 1 to 7, beginning with $3s_{1/2}\epsilon p_{1/2}$. Channels 1 and 2 are open, since the Mg^+ $3S$ limit at 61 671 cm^{-1} lies well below the term energy of the final, laser-excited state. Below the 97 340.3-cm^{-1} $3P_{1/2}$ limit, channels 3 through 7 are closed; above this energy channels 3 and 5 become open. The closed channels are characterized by effective quantum numbers with respect to their associated limits: $\nu_3(=\nu_5)$ for channels 3 and 5, and $\nu_4(=\nu_6=\nu_7)$ for channels 4, 6, and 7.

The electron plus ion system which results from the autoionization decay of the doubly excited state is termed a collision eigenstate. There are as many of these collision eigenstates, $\Psi^{(\rho)}$, as there are open channels, and each is a linearly independent combination of the open-channel wave functions. Corresponding to each of these states is a highly energy-dependent continuum phase $-\pi\tau_\rho$. There are as many of these collision eigenstates (and hence continuum phases) as there are open channels.

The wave function describing the ρth collision eigenstate may be expressed in terms of close-coupled wave functions $\psi_\alpha^{(\rho)}$ satisfying the $r=0$ boundary conditions, and dissociation wave functions $\phi_i^{(\rho)}$ satisfying the $r=\infty$ boundary conditions:

$$\Psi^{(\rho)}=\sum_i A_i\phi_i^{(\rho)}=\sum_\alpha B_\alpha\psi_\alpha^{(\rho)} \ . \tag{3}$$

Satisfying both boundary conditions leads to the condition[12]

$$\sum_i U_{i\alpha}\sin[\pi(\nu_i+\mu_\alpha)]A_i=0 \ , \tag{4}$$

where $U_{i\alpha}$ is a unitary transformation connecting the two basis sets, and the μ_α are the scattering phase shifts for the αth close-coupled channel. The ν_i are replaced by $-\tau_\rho$ for the open channels. The tan $\pi\mu_\alpha$ are the eigenvalues of the $\underline{K}$ matrix, which may be decomposed into

$$\underline{K}=\underline{U}(\tan\pi\boldsymbol{\mu})\underline{U}^T \ . \tag{5}$$

CC have rewritten Eq. (4) as

$$(\underline{K}+\tan\pi\boldsymbol{\nu})\mathbf{a}=0 \ , \tag{6a}$$

where

$$a_i=\cos(\pi\nu_i)A_i \ . \tag{6b}$$

The LL method described in some detail in I is particularly appropriate if one is interested in graphical representations of the interactions between well-specified channels (e.g. Lu-Fano plots[15]) or in the continuum phases. Alternatively, if the continuum phases are not of interest, the simplified version of the procedure described by CC can be used to very efficiently synthesize measured spectra. Since we are not concerned with the actual phases of the continua, we have used the CC method, and we outline it here.

CC shift the effective quantum numbers ν_i of the dissociation (or "collision") channels by the single-channel quantum defects δ_i, to yield integer-valued quantum numbers ν_i', and a shifted vector, $\mathbf{a}'$, viz

$$\nu_1'=\nu_i+\delta_i \ , \tag{7a}$$

$$a_i'=A_i\cos(\pi\nu_i') \ . \tag{7b}$$

The δ_i represent the core phase shifts experienced by the wave functions, and the shifts are introduced to both the open and closed channels. The δ_i also take into account the large quantum defects exhibited by many low-l states that are due to nonhydrogenic, spherical perturbations rather than channel mixing. With this transformation, Eq. (6a) can be rewritten as

$$[\underline{K}'+\tan(\pi\boldsymbol{\nu}')]\mathbf{a}'=0 \ . \tag{8}$$

CC give the transformation relating $\underline{K}'$ and $\underline{K}$. The sizes of the $\underline{K}'$ elements correspond to the extent of channel mixing.

In order to model the autoionizing state, it is convenient to subdivide $\underline{K}'+\tan(\pi\boldsymbol{\nu}')$ into bound-bound, bound-continuum, continuum-bound, and continuum-continuum quadrants:

$$\underline{K}'+\tan(\pi\boldsymbol{\nu}') = \begin{vmatrix} [\underline{K}'+\tan(\pi\boldsymbol{\nu}')]_{bb} & \underline{K}'_{bc} \\ \underline{K}'_{cb} & [\underline{K}'+\tan(\pi\boldsymbol{\nu}')]_{cc} \end{vmatrix} \ . \tag{9}$$

CC reduce the problem to an n_c-dimensional eigenvalue problem, where n_c is the number of continuum channels:

$$\{\underline{K}'_{cb}[\underline{K}'+\tan(\pi\boldsymbol{\nu}')]^{-1}_{bb}\underline{K}'_{bc}-\underline{K}'_{cc}\}\mathbf{a}'_c=\epsilon_j\mathbf{a}'_c\ , \tag{10a}$$

$$\mathbf{a}'_b=-[\underline{K}'+\tan(\pi\boldsymbol{\nu}')]^{-1}_{bb}\underline{K}'_{bc}\mathbf{a}'_c\ . \tag{10b}$$

The continuum eigenvectors are normalized according to

$$[(\epsilon_j)^2+1]\sum_{\{n_c\}}(a'_c)^2=1\ . \tag{11}$$

The spectral densities A_i corresponding to the closed (bound) channels may be evaluated from $\mathbf{a}'$ using Eq. (7b).

To match the ICE technique the amplitude D_ρ for excitation of collision eigenstate $\Psi^{(\rho)}$ from the initial Rydberg state $|a\rangle$ is given by a summation over the closed dissociation channels:

$$\begin{aligned}D_\rho&=\langle\Psi^{(\rho)}|\mathbf{r}|a\rangle\\&=\sum_{\{n_b\}}\langle i|\mathbf{r}|a\rangle A_i^{(\rho)}\ .\end{aligned} \tag{11$'$}$$

As discussed in I, each $\langle i|\mathbf{r}|a\rangle$ includes a factor proportional to the angular part of the dipole transition probability (e.g., $\langle 3p_{J_i}\nu'_{J_i}d_j|\mathbf{r}_\Omega|3s_{1/2}nd_j\rangle_{J=1}$), and a factor proportional to the "overlap" of the Rydberg electron's wave function before and after excitation of the second electron. For concreteness, the amplitude for excitation of the $3pns$ collision eigenstate $\Psi^{(\rho)}$ from the $3sns$ $^1S_0$ Rydberg state is expressed as

$$\begin{aligned}D_\rho=\langle 3p|\mathbf{r}_\mathbf{r}|3s\rangle[&-(\tfrac{1}{3})A_3^{(\rho)}\langle\nu'_{P_{1/2}}|\nu\rangle\\&+\sqrt{2/9}\,A_4^{(\rho)}\langle\nu'_{P_{3/2}}|\nu)]\ .\end{aligned} \tag{12}$$

where $\langle 3p|\mathbf{r}_\mathbf{r}|3s\rangle$ is the radial matrix element (constant for all Mg^+ $3s$-$3p$ transition), and $\langle\nu'_{P_{J_i}}\nu\rangle$ is the overlap integral between the outer-electron wave function in the bound $3sns$ state of effective quantum number ν and the autoionizing $3p_{J_i}\nu'$ state with effective quantum number ν'. The index i on A_i refers to the jj-coupled states enumerated in Eq. (1). The observed cross section for excitation of the doubly excited states is given by

$$\sigma=\mathrm{const}\times\omega\sum_{\rho=\{n_c\}}|D_\rho|^2\ , \tag{13}$$

where ω is the third laser frequency.

Although there is only one correct set of δ_i corresponding to the dissociation channels, any set of δ_i, including that with all $\delta_i\equiv 0$, will yield a correct final cross section σ. Setting the δ_i to arbitrary values effectively "rotates" the continuum and bound basis states ($\mathbf{a}'$) into new, complicated, linear combinations. In this study, we are only interested in the final cross section, rather than, for instance, the proportion of autoionizing occurring to a certain specified continuum. Numerical solution of the "correct" set of quantum defects in an N-channel system is a difficult procedure, particularly for moderately large N, since there will be N sets of δ_i satisfying Eq. (8), only one of which is physically meaningful. Setting all the δ_i to zero, and hence $\underline{K}'=\underline{K}$, markedly simplifies the computation involved in deducing σ.

As mentioned, we have used the CC procedure to synthesize the $J=1$ spectra. It yields spectra much more rapidly than the LL approach described in I. (As a check, we also calculated spectra using the latter method; the results were identical.) Of course, the LL method is the procedure of choice if one wishes to directly calculate the continuum phase τ_ρ, for example. However, such information is not necessary for synthesizing the spectra measured in this experiment.

RESULTS

Spectra of the Mg $3pnd$ states excited by linearly polarized laser light were measured for all n values between 9 and 40 inclusive. $3pns$ spectra were measured for $n=10$ to 18. Nonlinearities in these wavelength scans have been corrected, and they have been put on an absolute frequency scale, as discussed earlier. At several n values, scans were repeated with the third-laser beam attenuated by a factor of 2 or 4, yielding essentially no change in the line shapes and relative amplitudes. Thus nonlinear effects (e.g., depletion broadening[16] or optical saturation) caused by the third-laser intensity are negligible.

We first discuss the $3pnd$ results. The spectrally integrated $J=1$ and $J=3$ excitation amplitudes are equal for this linear-polarized scheme, although the $J=3$ features are generally broader and hence have smaller peak amplitudes than the $J=1$ features. The computed $J=1$ spectra were added to the previously calculated $J=3$ spectra to synthesize the signal expected with linear polarization.

Figure 4 shows spectra for $3pnd$ $n=20$ as a function of the third (scanning) laser frequency. It is evident from comparison of the combined $J=1$ and $J=3$ calculations and the $J=1$ spectra alone that the sharper peaks are identified with $J=1$. Also indicated in frame (a) of this figure are the energies of the Mg^+ $3P_{1/2}$ and $3P_{3/2}$ ion transitions.

The nonzero linewidth of the third dye laser broadens the sharp features and limits resolution of closely spaced peaks. Convolution of a Gaussian line shape having a full width at half maximum (FWHM) of 1.3 cm^{-1} with the computed spectra gives good agreement with the measured ion signals, as can be seen in Fig. 4(d). This linewidth is in accord with the expected linewidth of the frequency-doubled laser radiation, which is approximately $\sqrt{2}$ greater than the measured fundamental linewidth of $\simeq 0.8$ cm.$^{-1}$ For some scans, a somewhat smaller FWHM ($\simeq 1.1$ cm^{-1}) was found to give the best agreement, presumably due to the day-to-day variations in the dye-laser alignment and performance.

Figure 5 presents the measured $3p11d$ spectra, as well as calculated spectra for $J=1$ and 3 combined and with $J=1$ alone. The $J=3$ features are generally much broader, and result in a significant broadening of the combined spectra when added to the $J=1$ features, as seen in a comparison of Figs. 5(b) and 5(c). In Fig. 5, it is also apparent that the spectra are heavily perturbed, with no significant features lying near the location of the Mg^+ $3P_{3/2}$ resonance.

Figure 6 illustrates the measured and calculated $3p17d$ spectra, including the constituent $J=1$ spectral densities

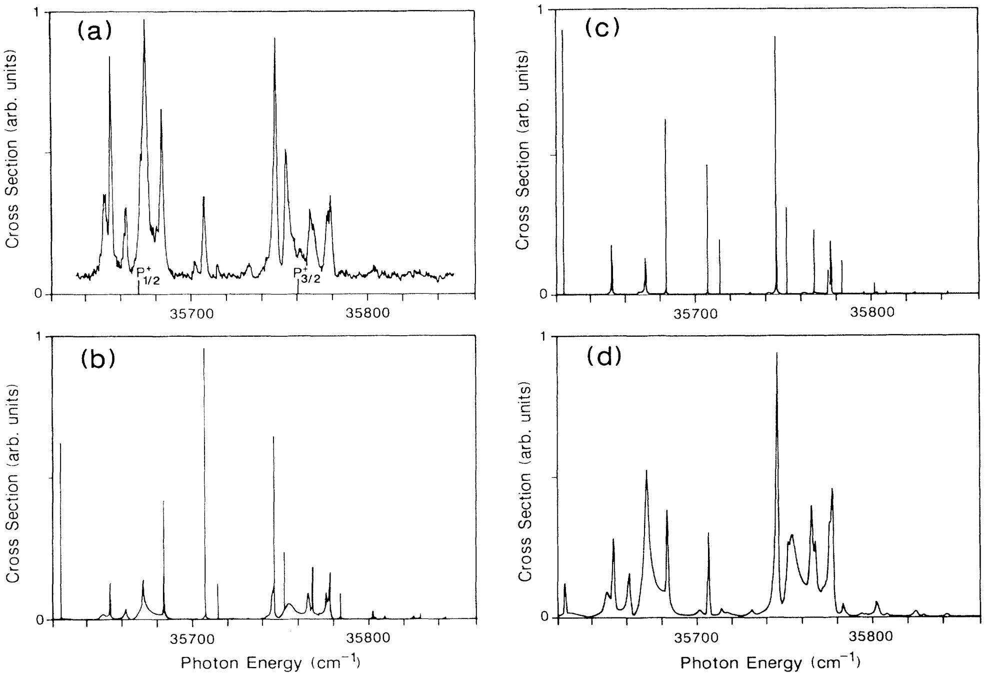

FIG. 4. $3p20d$ autoionization spectra: (a) detected ion signal following linear-polarized excitation; (b) associated synthetic spectrum combining both $J=1$ and $J=3$ final states; (c) synthetic spectrum for $J=1$ final state only. The energies of the Mg^+ $3p_{1/2}$ and $3P_{3/2}$ ion transitions are indicated on (a).

from which the synthesized spectrum is derived, as given by Eqs. (11) and (13). For $3pnd$, the relevant spectral densities are A_5, A_6, and A_7, although, in general, configuration interaction between series perturbs each spectral density so that no A_i is composed purely of its corresponding nominal $3p_j nl_j$ series.

As n increases, the spectral structure coalesces into two bundles associated with the $3S$-$3P_{1/2}$ and $3S$-$3P_{3/2}$ energies, respectively. Experimental and synthetic spectra of the $3p30d$ state are shown in Fig. 7. The instrumental linewidth is unfortunately too large to allow confirmation of the sharp structure seen in the calculations. As pointed out in I, the periodic structure superimposed on the Mg^+ $3P_{3/2}$ envelope is attributable to interseries interaction with the $3p_{1/2}nd_{3/2,5/2}$ series (Fig. 3). We note that the total area of the $3P_{3/2}$ bundle is approximately twice that of $3P_{1/2}$, as expected, since the former state has twice the degeneracy of the latter.

Above $n=35$, the $3p_{3/2}$ doubly excited states lie above the $3P_{1/2}$ limit, and hence no longer exhibit detailed structure due to the interaction with the $3p_{1/2},ns_{1/2}$ and $3p_{1/2}nd_{3/2,5/2}$ series. Above the $3P_{1/2}$ limit the same interaction, presumably the electric-quadrupole interaction,[17] exists with the $3p_{1/2}\epsilon s_{1/2}$ and $3p_{1/2}\epsilon d_{3/2,5/2}$ continua, and we expect the envelopes of the observed spectra to be the same just above and just below the $3P_{1/2}$ limit. Experimentally, the measured spectra from $n=32$ to 40 appear nearly identical.

Measurement of the $3pns$ spectra is experimentally more difficult than the $3pnd$ spectra. The $3s3p$-$3sns$ transitions are inherently much weaker than their $3s3p$-$3snd$ counterparts, making these states difficult to populate.

TABLE II. Measured energies and corresponding quantum defects for Mg $3sns$ $^1S_0$ Rydberg series. The quantum defects are calculated with respect to the 61 671.02 cm⁻¹ first ionization limit.[a] Estimated statistical measurement errors are given for the energies, along with their propagation into the quantum-defect values.

n	Term energy (cm⁻¹)	Quantum defect
10	60 143.30(7)	1.5248(2)
11	60 448.95(8)	1.5240(3)
12	60 670.84(8)	1.5255(4)
13	60 837.86(9)	1.5235(6)
14	60 965.86(8)	1.5253(7)
15	61 067.14(9)	1.520(1)
16	61 147.99(9)	1.515(1)
17	61 213.08(9)	1.520(2)
18	61 266.75(9)	1.525(2)
19	61 311.5(1)	1.529(2)
20	61 349.0(1)	1.540(3)
21	61 381.4(1)	1.535(3)
22	61 408.9(1)	1.539(4)

[a] See Ref. 18.

Moreover, the quantum defects of the 3*sns* and 3*snd* states are ~1.55 and ~0.55, respectively. For $n > 22$, this difference becomes very close to unity. The 3*sns* state is thus nearly degenerate with the $3s(n-1)d$ state, precluding excitation of resolvable high-*n* 3*pns* doubly excited states.

To our knowledge, experimentally determined energies of the Mg 3*sns* $^1S_0$ Rydberg-state energies have been published only up to $n = 10$.[18] In order that the second laser (Fig. 2) could be readily tuned to the appropriate wavelength, we measured the 3*sns* energies by scanning this laser over a wide range and used field ionization to detect the populated states. The results of these measurements are presented in Table II, along the associated quantum defects.

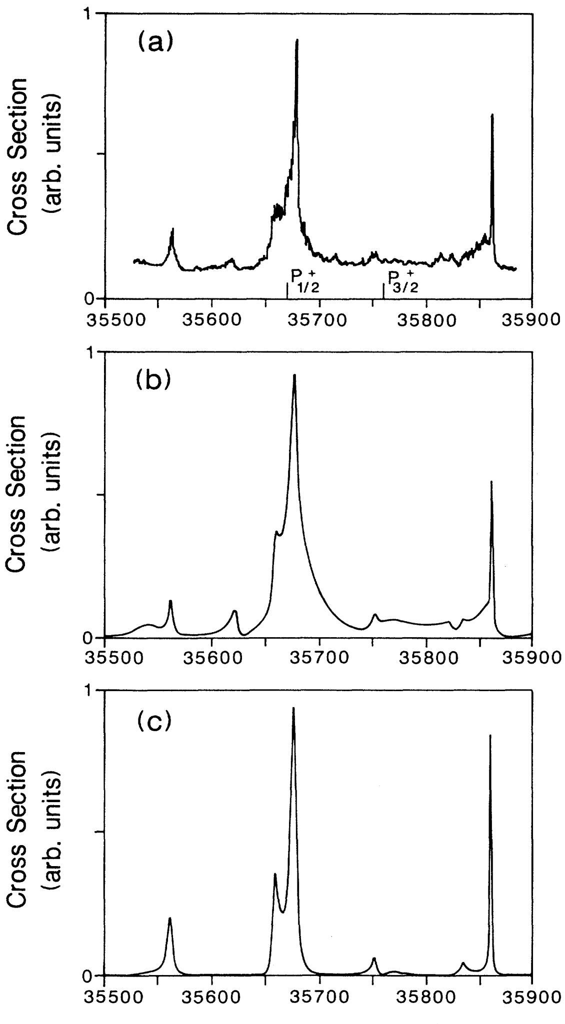

FIG. 5. $3p11d$ autoionization spectra: (a) measured; (b) combined calculated $J=1$ and $J=3$ spectra for the same state; (c) $J=1$ spectrum alone.

Figure 8 shows measured and calculated spectra for $3p11s$, and Fig. 9 presents the results for $3p15s$. The signal-to-noise ratio is poorer and the features are generally broader than that found in their 3*pnd* counterparts.

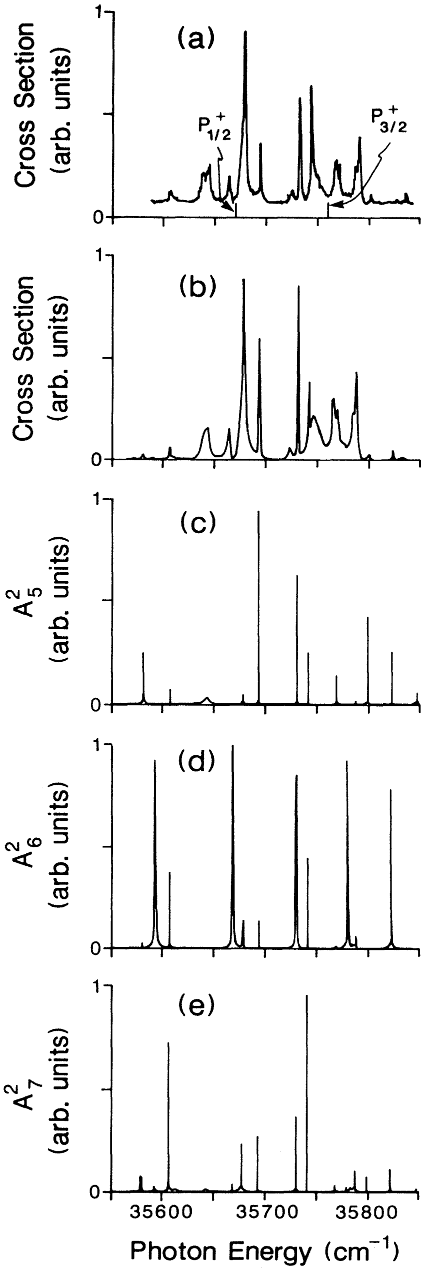

FIG. 6. $3p17d$ autoionization: (a) measured; (b) calculated, including both $J=1$ and $J=3$ contributions and linewidth convolution; (c)–(e) spectral densities A_i^2 corresponding to $3p_{1/2}nd_{3/2}$, $3p_{3/2}nd_{3/2}$, and $3p_{3/2}nd_{5/2}$ $J=1$ series. Each spectral density A_i must be multiplied by the appropriate angular momentum and overlap-integral coefficient, and the resultant sum squared to give $|D_\rho|^2$, which when summed over ρ, yields the cross section to within a constant factor.

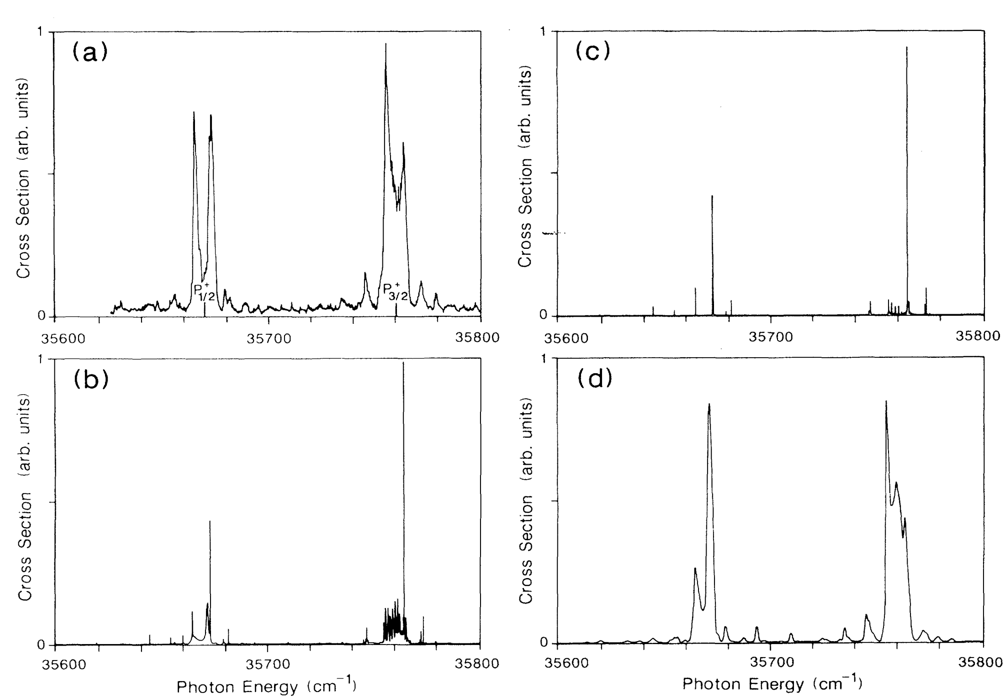

FIG. 7. $3p30d$ autoionization spectra: (a) measured; (b) combined $J=1$ and $J=3$ synthesized spectra; (c) $J=1$ synthesized spectrum only; (d) same as (b), but with convolution of nonzero instrumental linewidth.

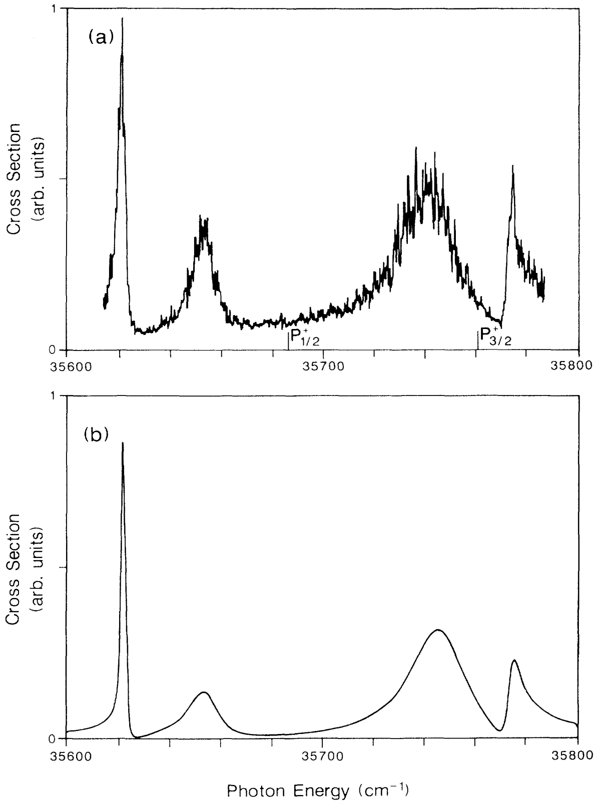

FIG. 8. The transition rate for excitation of the 3*sns* Rydberg states is much lower than that for the corresponding 3*snd* states. As a result, the 3*pns* spectra exhibit much poorer signal-to-noise ratios. Shown are the (a) measured and (b) calculated $3p11s$ spectra.

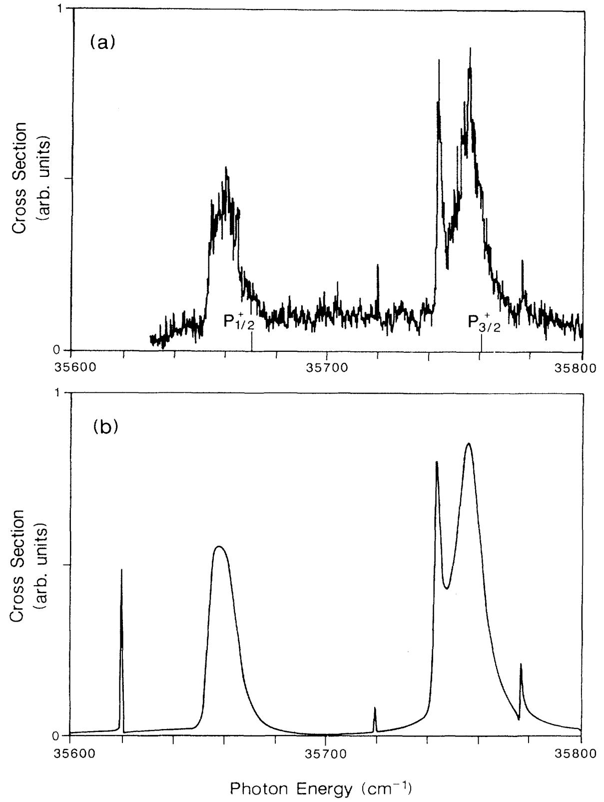

FIG. 9. $3p15s$ autoionization spectra: (a) measured, (b) calculated. Note that the main features correspond more closely to the ion-line positions than those in Fig. 8. This is a general trend for 3*pnl* states as *n* increases, since the outer electron plays more the role of a spectator.

DISCUSSION

As noted, the 3*pns* spectra are characterized by much broader (i.e., shorter-lifetime) features than those in the 3*pnd* ($J=1$) spectra. Similarly, the 3*pnd* $J=3$ spectra have broader peaks than those found in 3*pnd* ($J=1$). Simple arguments can qualitatively explain these differences.

First let us consider the 3*pnd* states. Figure 10 schematically illustrates the potential curves and hydrogenic radial wave functions of the outer electron associated with the 3*pnd* doubly excited states, and the $3s\epsilon p$ and $3s\epsilon f$ continua. As a result of the centrifugal barrier, $V_c=[l(l+1)]/2r^2$, the first node of the radial wave function occurs at increasing *r* with increasing *l*. One would, as a result, expect the *d* wave shown in Figure 10 to be intermediate between the *p* and *f* waves. It is not, but similar to the *f* wave because the excitation of the 3*p* ionic core leaves much less energy for the Rydberg *nd* electron, compensating for the difference in the centrifugal barriers. As seen in Fig. 10, the overlap between the 3*pnd* and $3s\epsilon f$ radial wave functions is substantially better than that between the 3*pnd* and the $3s\epsilon p$ radial wave functions, leading to higher autoionization rates of $J=3$ states and wider $J=3$ spectral features.

Although we have not shown the radial wave function for the 3*pns* states, it overlaps the $3s\epsilon p$ radial wave function well, with a spatial overlap comparable to the 3*pnd*-$3s\epsilon f$ overlap shown in Fig. 10. The fact that the overlap occurs at smaller radius, however, means that the 3*pns* states have faster autoionization rates than the 3*pnd* ($J=3$) states.

These arguments emphasize that although the Rydberg electron is localized at large *r*, it is the small fraction of its wave function near the core which determines the autoionization properties of the atom.

The $3P_{1/2}$-$3P_{3/2}$ fine-structure separation of the Mg^+ first-resonance state is $\simeq 92\ \mathrm{cm}^{-1}$, considerably less than the first-resonance splitting of the heavier alkaline-earth elements (cf. 220 cm^{-1} in Ca^+, $\sim 800\ \mathrm{cm}^{-1}$ in Sr^+, and $\sim 2000\ \mathrm{cm}^{-1}$ in Ba^+). As discussed in some detail in I, this difference can lead to marked interference effects. Described somewhat simplistically, if the 3*snl* Rydberg atom is excited by a photon having an energy corresponding to the Mg^+ $3S$-$3P_{3/2}$ transition, the inner electron may be excited to $3P_{3/2}$, or it may be excited to $3P_{1/2}$, with the outer electron simultaneously changing to an orbit with higher *n* (and hence greater energy). Since both of these processes lead to autoionization and the same final continuum-electron–core configuration, their respective amplitudes can interfere. The probability that the Rydberg electron may adjust its orbit as the inner electron is excited is given by an "overlap integral."[19,20] This probability is significantly enhanced when the energy spacing between successive Rydberg states approximately matches the ion fine-structure splitting. In Mg, this match occurs for $n\sim 14$, and in this *n* region the spectra indeed exhibit noticeable interference effects.

"Overlap interference" may be viewed alternatively as

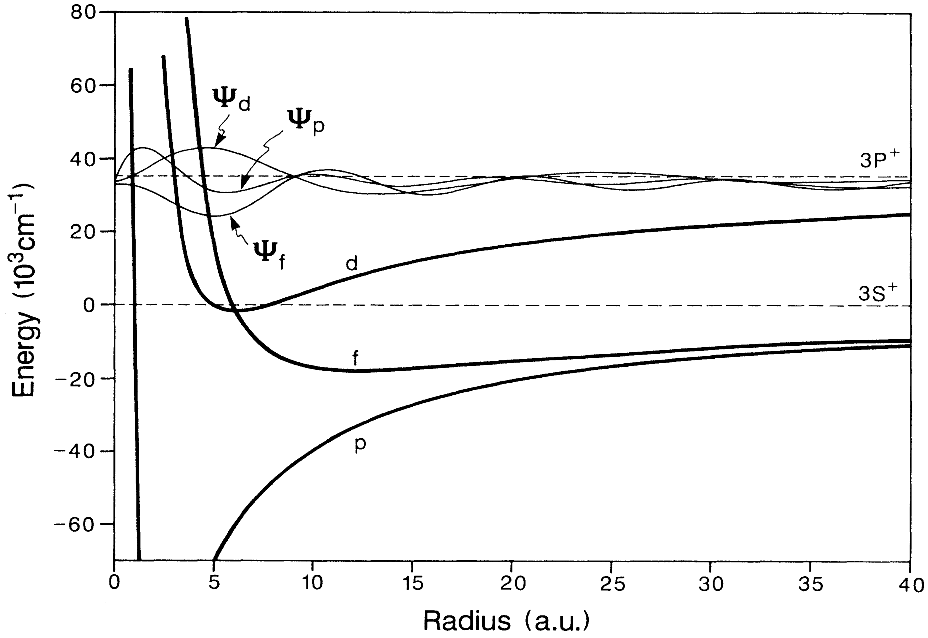

FIG. 10. Qualitative illustration of the Rydberg-electron potential curves and wave functions appropriate to 3*pnd* excitation. The potential curves are calculated using only the Coulomb and centrifugal-barrier terms. The *d* potential converges to the Mg^+ 3*p* limit, to which the 3*pnd* members converge. The wave functions are hydrogenic wave functions calculated using Numerov integration. As discussed in the text, wave-function-overlap considerations can explain the generally broader nature of the $J=3$ features compared with $J=1$.

the transition from the *jj*-coupled representation most appropriate for the high-*n* autoionizing Rydberg series to *LS*-coupling as *n* decreases. The Hamiltonian for this two-electron atom has the form

$$H=H_0+\frac{1}{|\mathbf{r}_1-\mathbf{r}_2|}+k\mathbf{L}\cdot\mathbf{S}\ , \tag{14}$$

where H_0 is the Hamiltonian of the atomic core. The second term on the right side represents the electrostatic repulsion between the two valence electrons. The spherical-harmonic expansion of this electrostatic interaction yields a lowest-order term representing the Coulomb potential experienced by the screened outer electron. This potential determines the spacings between successive Rydberg states. For *n* values at which these

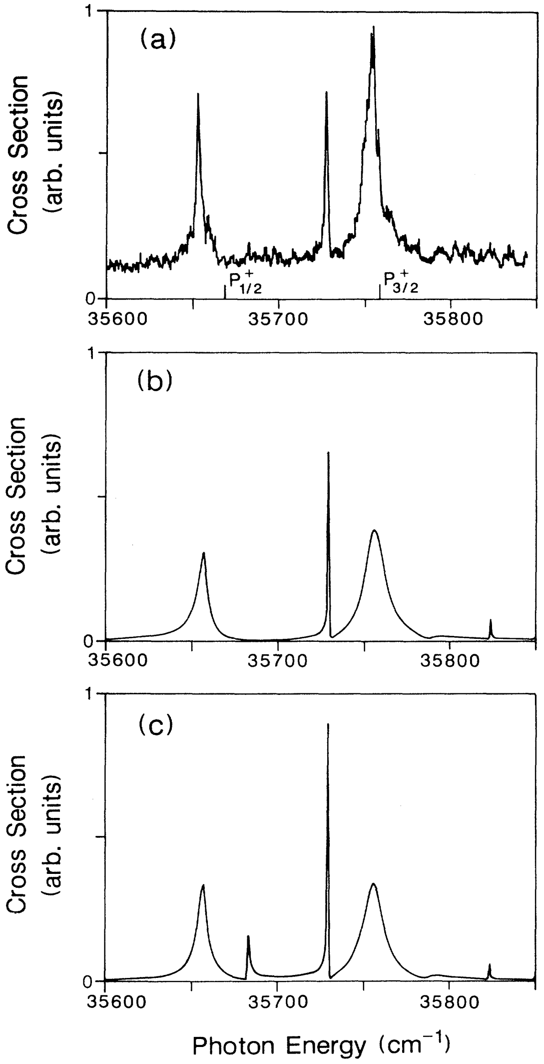

FIG. 11. 3*p*13*s* autoionization spectrum: (a) measured; (b) calculated (without linewidth convolution); (c) calculated using only "direct" excitation (without linewidth convolution).

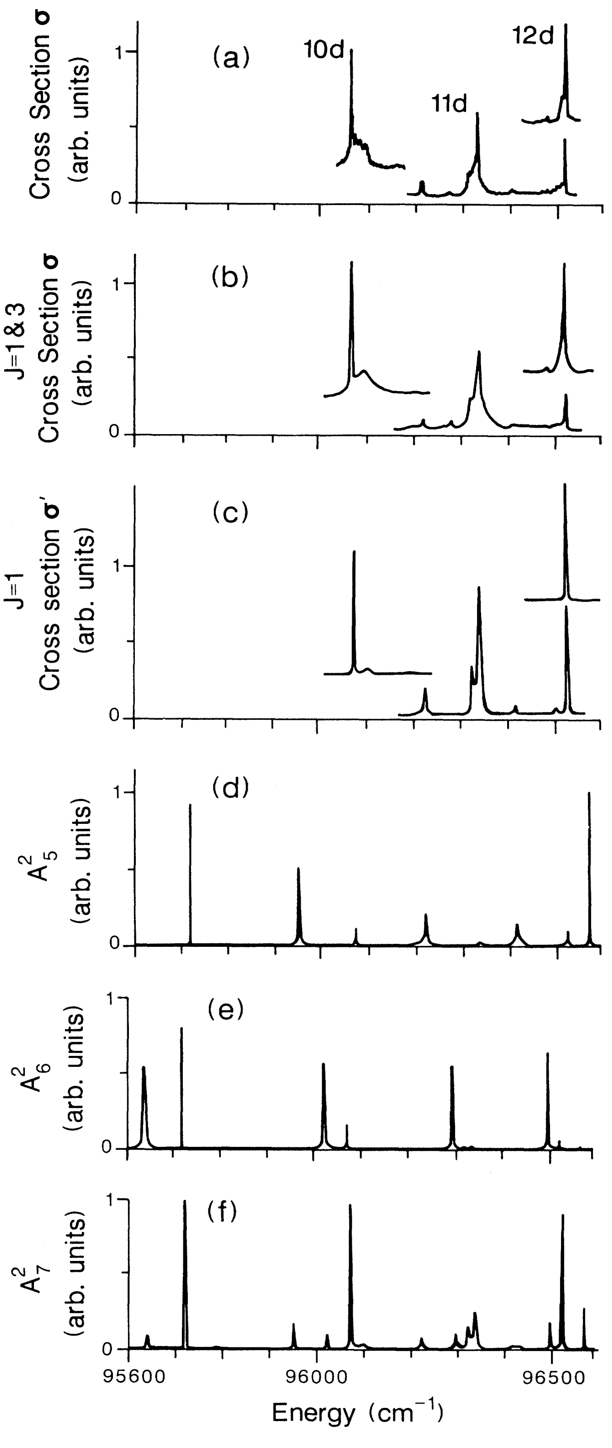

FIG. 12. Illustration of classification of the observed features in terms of the calculated constituent spectral density. The spectral density is calculated over a wide range, and the $J=1$ spectra of frame (c) are synthesized in accordance with the prescription outlined in the text. A similar procedure is used to evaluate the $J=3$ spectra for the 3*pnd* states, and the combined result is shown in (b). The measured spectra are indicated in the uppermost frame. Some peaks in the final spectra originate from common features in the spectra density.

spacings are approximately equal to the ion first-resonance fine-structure splitting (determined by the $\mathbf{L}\cdot\mathbf{S}$ term in the Hamiltonian), the basis representation is intermediate between the two coupling schemes. Since $\mathbf{L}\cdot\mathbf{S}$ is larger in the heavier alkaline-earth-metal elements, this intermediate representation occurs at lower n values than normally important in most previous alkaline-earth-metal ICE studies.

The importance of this interference effect may be quantified by squaring each D_ρ given by Eq. (12), and denoting the cross term in the expansion as $(D_\rho)_{\text{int}}$, and the remaining terms as $(D_\rho)_{\text{dir}}$. Thus each squared amplitude in Eq. (13) may be written as the sum of direct and interference terms:

$$(D_\rho)^2=[(D_\rho)_{\text{dir}}]^2+[(D_\rho)_{\text{int}}] \; . \tag{15}$$

In the absence of overlap interference, the last term in this equation would be zero. Figure 11 illustrates the contribution of interference to the $3p13s$ spectra. Figure 11(c) shows the spectra calculated using only the direct terms, and exhibits a distinct asymmetric peak at 35 684 cm^{-1} not seen in either the final calculated spectrum (b) or measurements (a).

In I, we identified the major observed spectral features comprising the $J=3$ closed channels by making use of the regularity of the associated quantum defects. In both the $J=1$ and $J=3$ systems, there are four "effective" quantum numbers (below the Mg^+ $3P_{1/2}$ limit): $\nu_{1/2}$ with respect to the $3P_{1/2}$ limit, $\nu_{3/2}$ with respect to the $3P_{3/2}$ limit, and the two continuum phases τ_ρ with respect to the Mg^+ $3S_{1/2}$ limit. A Lu-Fano plot of $\text{mod}(\nu_{1/2})$ versus $\text{mod}(\nu_{3/2})$ constructed from these $J=3$ data showed strong interseries interaction. However, its essential regularity indicated that the underlying continua phases maintained a relatively stable value for all of the observed features, or, more accurately, that the rate of change of these phases was greatest at a nearly constant τ value. In I, a three-dimensional model was invoked to illustrate geometrically the significance of this narrow range of τ values.

We attempted to perform a similar classification of the $J=1$ data. In order to aid in the identification of the observed peaks (obviously further complicated by the presence of $J=3$ features in the measured spectra), we used the spectral densities calculated over a wide energy range. As mentioned earlier, for $3pns$ these spectral features arise from A_3 and A_4, and for $3pnd$ the relevant spectral densities are A_5, A_6, and A_7. For low and intermediate n values (<30), individual features in the observed spectra can be associated with a particular A_i, and hence, at least nominally, with a particular series (Fig. 12). Note that certain peaks, as for example one observed in the $3p12d$ spectrum, are also observed in the $3p11d$ spectrum.

After the term energies of many $J=1$ features were classified, the quantum defects were not found to follow an obvious pattern. An attempt to construct a Lu-Fano plot analogous to that in I using the present $J=1$ data yields a seemingly nearly random distribution of points. From this, one infers that the underlying continuum phases do not remain constant for the $J=1$ features.

The overall agreement found between experiment and the results of the reaction-matrix calculations is striking. Nevertheless there are some persistent deviations between theory and experiment which cannot be simply attributed to experimental uncertainty.

For instance, the depth of the trough in the large $3p15s$ feature (Fig. 9) near the Mg^+ $3P_{3/2}$ transition line is markedly greater in the experimental data than in the theoretical spectrum. Similarly, the calculated width of the highest-energy feature in the $3p13s$ spectrum of Fig. 11(b) is significantly greater than the measured width of Fig. 11(a). Moreover, for $3p10s$, the lowest measured $3pns$ state, there is significant disagreement not only in the widths of several features but also in their energies.

Some discrepancies are also manifest in the data for some of the $3pnd$ states. The disagreements seen in comparison of frames (a) and (d) in the $3p30d$ spectra of Fig. 7 are qualitatively alike those seen in spectra of nearby n. Similar disagreements between theory and experiment were seen in the $J=3$ data presented in I.

CONCLUSIONS

We have studied in some detail the $3pns$ and $3pnd$ ($J=1$) autoionizing doubly excited states for a wide range of n, across which the behavior of the observed spectra changes substantially. These n-dependent changes in behavior can be explained using simple physical models, as can the qualitative differences in linewidth between the $3pnd$ $J=1$ and $J=3$ states, and between the $3pns$ and $3pnd$ $J=1$ states. In addition, the comparatively complex measured spectra have been well reproduced using a reaction-matrix method.

This work underscores the essential validity and utility of the reaction-matrix approach. However, the relatively minor deviations between theory and experiment point out possibilities for refinement of the model. This work, in conjunction with the earlier work in I, provides a sensitive test of the applicability of the theory to a light alkaline-earth-metal element such as Mg.

Study of the $3pns$ autoionizing states is especially appealing, since $J=1$ is the only allowed final excited-state angular momentum. Thus it is in many ways a "complete" system. Furthermore, the core-penetrating character of s-wave functions renders the study of $3pns$ states a more stringent test of the reaction-matrix model. Work is currently underway to study the angular dependence of the autoionizing electrons for this system, which should be a further, more sensitive test.

ACKNOWLEDGMENTS

It is a pleasure to acknowledge very helpful discussions with R. R. Jones, W. Sandner, and J. C. Camparo. We are grateful to C. H. Greene for providing us with his Mg K matrices prior to publication, without which synthesis of the spectra would not have been possible. This work has been supported by the U. S. Department of Energy, Division of Chemical Sciences, Office of Basic Energy Sciences.

[1] J. J. Wynne and J. A. Armstrong, Comments At. Mol. Phys. **8**, 155 (1979).

[2] W. Sandner, Comments At. Mol. Phys. **20**, 171 (1987).

[3] C. J. Dai, G. W. Schinn, and T. F. Gallagher, Phys. Rev. A **42**, 223 (1990).

[4] W. E. Cooke, T. F. Gallagher, S. A. Edelstein, and R. M. Hill, Phys. Rev. Lett. **40**, 178 (1978).

[5] U. Fano, Phys. Rev. **124**, 1866 (1961).

[6] C. H. Greene and Ch. Jungen, Adv. At. Mol. Phys. **21**, 51 (1985).

[7] V. Lange, U. Eichmann, and W. Sandner, J. Phys. B **22**, L245 (1989).

[8] M. Aymar and J. M. Lecomte, J. Phys. B **22**, 223 (1989).

[9] V. Lange, M. Aymar, U. Eichmann, and W. Sandner (unpublished).

[10] C. H. Greene (private communcation).

[11] C. H. Greene and L. Kim, Phys. Rev. A **36**, 2706 (1987).

[12] W. E. Cooke and C. L. Cromer, Phys. Rev. A **32**, 2725 (1985). Note that their $\underline{R}$ and $\underline{R}'$ matrices correspond to our $\underline{K}$ and $\underline{K}'$ matrices, respectively.

[13] C.-M. Lee and K. T. Lu, Phys. Rev. A **8**, 1241 (1973).

[14] R. D. Cowan, *The Theory of Atomic Structure and Spectra* (University of California Press, Berkeley, 1981).

[15] K. T. Lu and U. Fano, Phys. Rev. A **2** 81 (1970).

[16] W. E. Cooke, S. A. Bhatti, and C. L. Cromer, Opt. Lett. **7**, 69 (1982).

[17] S. M. Jaffe, R. Kachru, H. B. van Linden van den Heuvell, and T. F. Gallagher, Phys. Rev. A **32**, 1480 (1985).

[18] W. C. Martin and R. Zalubas, J. Phys. Chem. Ref. Data **9**, 4 (1980).

[19] S. A. Bhatti, C. L. Cromer, and W. E. Cooke, Phys. Rev. A **24**, 161 (1981).

[20] T. F. Gallagher, J. Opt. Soc. Am. B **4**, 794 (1987).